NTNU
Kunnskap for en bedre verden

Department of Engineering Cybernetics

TTK4550 - Specialization Project

Radar-Inertial Navigation for Resilient Odometry

Author:
Nicolai Adil Øyen Aatif

Supervisors:
Kostas Alexis
Morten Nissov

December, 2025

Abstract

Reliable odometry is fundamental for autonomous navigation; however, most estimation pipelines degrade rapidly in geometric self-similar environments and in conditions with dense obscurants, such as dust, fog, or smoke, particularly when Global Navigation Satellite System (GNSS) measurements are unavailable. While Inertial Navigation Systems (INS) provide high-rate motion tracking, they suffer from unbounded drift when unaided. Frequency-Modulated Continuous-Wave (FMCW) radars, in contrast, provide range and radial speed information independent of illumination and adverse visibility conditions, making it an attractive complementary modality.

This work proposes a tightly coupled radar-inertial odometry method that exploits radial speed measurements from an FMCW radar. Each radar detection provides an aiding measurement along its line-of-sight, directly relating the measured radial velocity to the vehicle's ego-motion under the assumption of a static environment. These per-point radial speed observations are fused with inertial measurements within an Error-State Kalman Filter (ESKF) framework, maintaining computational efficiency while improving state observability.

Experimental evaluation shows that radial speed measurements effectively aid translational motion and improve short-term navigation accuracy. The Relative Pose Error (RPE) remains low across all datasets, indicating good local consistency of the estimated motion. All datasets exhibit vertical and yaw drift, with the former being more pronounced. Overall, the results show that per-point radar radial speed aiding significantly enhances local inertial navigation performance, while long-term accuracy remains limited by the absence of absolute position, heading information or loop closures.

Contents

List of Figures

List of Tables

1 Introduction

1.1 Context and Motivation

Reliable state estimation is a fundamental requirement for autonomous robots, especially in situations where GNSS measurements are unavailable, unreliable, or intentionally denied. In such scenarios, inertial navigation systems are commonly used due to their high update rates and low price. However, INS solutions inevitably suffer from drift caused by sensor noise and slowly varying biases, making additional aiding sources necessary for sustained operation.

Vision-based sensors are often employed to aid INS [1], but their performance degrades in low-light conditions, visually sparse environments, or in the presence of dust, fog, or smoke. Radar sensors offer complementary characteristics, providing robustness to lighting and weather conditions [2]. In particular, FMCW radars can measure radial velocities through the Doppler effect, offering direct motion-related information that is well-suited for aided inertial navigation.

Recent advances in compact radar hardware have made it feasible to integrate radar sensors on small aerial platforms. This motivates the investigation of radar–inertial sensor fusion methods that can exploit radial speed measurements to reduce inertial drift while retaining robustness across a wide range of operating conditions. Several recent works exploit Doppler information from FMCW radars to aid inertial state estimation. The work in [3] fuses per-point radar radial speed measurements with inertial and LiDAR data, while [4] estimates a single linear velocity which is fused, both in a factor-graph framework. Another approach is to use landmark-based methods, as in [5], which require structured environments and feature extraction. More recently, attention has also shifted toward practical challenges in radar-inertial fusion such as time synchronization. In addition to estimating the motion of the system, [6] also estimates the temporal offset between the radar and the Inertial Measurement Unit (IMU). Overall, existing literature demonstrates that radar Doppler information is a valuable aiding source for inertial navigation.

1.2 Problem Description

This work addresses the problem of estimating the state of an aerial vehicle using measurements from an IMU and an FMCW radar. The estimated state comprises position, velocity, orientation, inertial sensor biases, and the extrinsic transformation between the radar and the IMU.

The FMCW radar provides per-detection radial speed measurements obtained from the Doppler effect. Each measurement relates the vehicle's motion to a specific line-of-sight direction defined by the corresponding radar detection. Although these measurements do not directly observe position or the full three-dimensional velocity vector, they provide motion-related information through the radar measurement geometry and the radar-IMU extrinsic parameters.

State estimation is formulated within an Error-State Kalman Filter (ESKF) framework. The nominal state is propagated using inertial navigation equations driven by IMU measurements, while radar radial speed measurements are incorporated through the measurement update. The information introduced by these updates depends on the vehicle's motion and on the availability and spatial distribution of radar detections, which together determine how informative each update step is.

1.3 Contributions and Scope

The main contributions of this work are as follows:

- The formulation and implementation of a radar–inertial ESKF using per-detection radial speed measurements,

- Analytic derivation of the radar measurement Jacobians, including terms related to inertial

states and radar extrinsic parameters, with numerical validation,

- Experimental evaluation on real flight data with different motion profiles, highlighting estimator performance, observability properties, and limitations.

The focus of this work is on estimator formulation, implementation, and experimental analysis. While several limitations are identified, addressing them through the use of additional sensors or alternative modeling choices is outside the scope of the current work and is instead discussed as future work.

The scope of this work is limited to radar radial speed aiding in a static environment. No absolute position measurements are assumed, and no explicit handling of dynamic objects is performed. Ground truth information is used exclusively for evaluation and is not available to the estimator.

The remainder of this thesis is organized as follows. Chapter 2 gives an introduction to the necessary theory. Chapter 3 presents the estimator formulation and implementation details. Chapter 4 evaluates the estimator on experimental datasets and discusses the observed behavior, and Chapter 5 concludes the thesis and outlines directions for future research.

1.3.1 Notation

The following coordinate frames are used in this work:

- W: Static world frame (World).
- I: Body-fixed IMU frame (IMU).
- R: Body-fixed radar frame (Radar).

Where the notation is adopted from [3, 4]. The position of frame A in frame B is given by ${}_{B}\mathbf{p}_{AB}$, and the rotation from frame A to frame B is given by ${}_{B}\mathbf{R}_{A}$. The same convention is used for velocities and other vector quantities where appropriate.

Furthermore, the variables x, $\mathbf{x}$, $\mathbf{X}$ are scalar, vector and matrix respectively.

2 Theory

2.1 FMCW Radar Fundamentals

Millimeter-wave (mmWave) FMCW radars are active sensors used to estimate the range, angle, and radial velocity of objects by transmitting electromagnetic signals and measuring their reflections. In contrast to passive sensors, FMCW radars emit their own signals and analyze how these signals are modified after reflecting from the environment. Spatial information is obtained from signal timing and antenna geometry, while motion information is obtained through the Doppler effect. FMCW radars are commonly operated at frequencies in the 76–81 GHz range [2], but systems in the 60–64 GHz band are also widely used and rely on the same physical measurement principles [7].

An FMCW radar transmits a sequence of signals with linearly increasing instantaneous frequency, referred to as chirps and shown in Fig. 1. When a chirp is reflected by an object, the received signal arrives delayed in time and may also be affected by a frequency shift if the object is moving. By mixing the transmitted and received signals, an intermediate-frequency (IF) signal is obtained. Information about range, radial velocity, and angle can then be extracted from the frequency and phase of this IF signal.
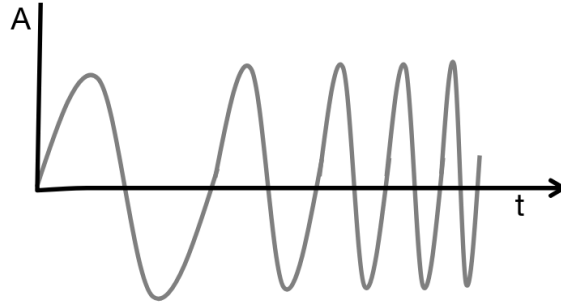
Figure 1: Chirp signal, with amplitude as a function of time. Figure taken from [8]
.

The time delay between transmitting a chirp and receiving its reflection is related to the distance of the object. Since the signal travels from the radar to the object and back, the delay is given by

$$\tau = \frac{2d}{c}, \tag{1}$$

where d is the distance to the reflecting object and c is the speed of light [8]. Estimating this delay is the basis for range estimation.

For a single stationary target, the received signal can be modeled as a sinusoidal signal with constant amplitude,

$$S_{\text{RX}}(t) = A \sin(2\pi f_0 t + \phi_0), \tag{2}$$

where A is the signal amplitude and

$$f_0 = S\tau, \qquad \phi_0 = \frac{4\pi d}{\lambda}.$$

Here, S denotes the chirp slope and λ is the wavelength of the transmitted signal. The frequency f_0 depends on the signal delay and is directly related to the object distance. Range estimation is performed by analyzing the frequency content of the IF signal over time [8].

If the object is moving relative to the radar, the received signal is additionally affected by the Doppler effect. This introduces a phase change in the received signal between consecutive chirps. Let $\Delta\phi$ denote the phase difference of the received signal corresponding to a fixed range bin in two consecutive chirps, and is given by

$$\Delta\phi = \frac{4\pi v T_c}{\lambda}, \tag{3}$$

where T_c is the time interval between the start of consecutive chirps [8], and v is the radial speed due to the Doppler effect. Solving for the radial speed yields

$$v = \frac{\lambda}{4\pi T_c} \Delta\phi. \tag{4}$$

In practice, the received signal contains reflections from multiple objects that might be at the same range. Rather than analyzing each chirp separately, the received signal is processed over a sequence of consecutive chirps. By analyzing how the signal phase evolves over time, reflections from objects with different radial velocities can be separated and estimated. A similar approach is used across multiple receive antennas, where phase differences between antenna elements are exploited to estimate the angle of arrival of the reflected signals.

2.2 Lie Theory

Robotic state estimation frequently involves quantities that do not live in Euclidean vector spaces. In particular, orientations and poses are constrained objects that evolve on nonlinear spaces. Treating them as vectors leads to inconsistencies when performing perturbations, averaging, or uncertainty propagation. Lie group theory provides a mathematically consistent framework for representing such states and their small variations, while still allowing local linearization.

2.2.1 Lie Groups and Manifolds

A group is a set equipped with a binary operation that satisfies closure, associativity, the existence of an identity element, and the existence of inverses. A manifold is a space that locally resembles an Euclidean space but may be globally curved [9]. Fig. 2 shows a Lie group (manifold) with its corresponding Lie algebra (tangent space).
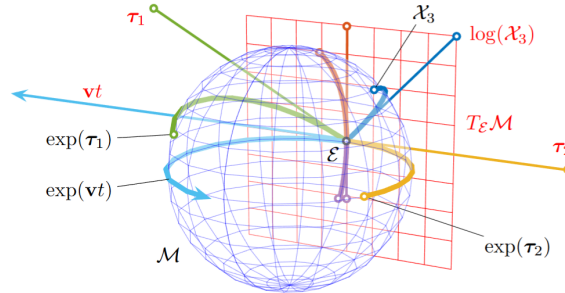
Figure 2: The Lie group (blue) and its Lie algebra (red). The sphere is used purely as a visual aid; it is not a Lie group, since a Lie group structure would require four dimensions. Figure taken from [10].

A Lie group is both a group and a smooth manifold, meaning that the group operations are smooth and differentiable. This allows calculus to be performed on the group. In robotics, Lie groups are used to represent rotations and rigid-body transformations.

The group of three-dimensional rotations is the special orthogonal group SO(3) given by

$$\mathrm{SO}(3) = \left\{ \mathbf{R} \in \mathbb{R}^{3\times 3} \mid \mathbf{R}^\top \mathbf{R} = \mathbf{I},\ \det(\mathbf{R}) = 1 \right\}. \tag{5}$$

Where $\mathbf{I}$ is the identity matrix.

2.2.2 Tangent Space and Lie Algebra

To perform estimation and uncertainty propagation, small perturbations of a rotation are represented in the tangent space of the manifold. For Lie groups, the tangent space at the identity element forms a tangent space known as the Lie algebra.

The Lie algebra associated with $SO(3)$ is denoted $\mathfrak{so}(3)$ and can be written as

$$\mathfrak{so}(3) = \left\{ \boldsymbol{\phi}^\wedge \in \mathbb{R}^{3\times 3} \,\middle|\, \boldsymbol{\phi}^\wedge = [\boldsymbol{\phi}]_\times = \begin{bmatrix} 0 & -\phi_3 & \phi_2 \\ \phi_3 & 0 & -\phi_1 \\ -\phi_2 & \phi_1 & 0 \end{bmatrix}, \, \boldsymbol{\phi} \in \mathbb{R}^3 \right\}. \tag{6}$$

where $\phi = \begin{bmatrix} \phi_1 & \phi_2 & \phi_3 \end{bmatrix}^\top$. The mapping between vector and matrix representations is defined through the hat and vee operators,

$$(\cdot)^\wedge : \mathbb{R}^3 \to \mathfrak{so}(3), \qquad (\cdot)^\vee : \mathfrak{so}(3) \to \mathbb{R}^3.$$

Elements of the Lie algebra are mapped to the Lie group using the exponential map,

$$\mathbf{R} = \exp\left(\boldsymbol{\phi}^\wedge\right),$$

while the logarithmic map provides the inverse mapping.

2.2.3 Plus and Minus Operators on Lie Groups

For states evolving on a Lie group $\mathcal{M}$, standard addition and subtraction are not defined globally. Instead, differences and increments are expressed using mappings between the manifold and its tangent spaces. These mappings are formalized through the plus ($\oplus$) and minus ($\ominus$) operators [10].

Let $\mathcal{X} \in \mathcal{M}$ denote a group element and let $\boldsymbol{\phi} \in T_\mathcal{X}\mathcal{M}$ be a vector in the tangent space at $\mathcal{X}$. In a right-invariant formulation, the plus operator is defined as

$$\mathcal{Y} = \mathcal{X} \oplus {}^\mathcal{X}\boldsymbol{\phi} \triangleq \mathcal{X} \circ \mathrm{Exp}({}^\mathcal{X}\boldsymbol{\phi}), \tag{7}$$

where $\circ$ denotes the group composition operator and $\mathrm{Exp}(\cdot)$ is the exponential map from the Lie algebra to the Lie group.

The corresponding minus operator maps two elements of the Lie group to a vector in the tangent space at $\mathcal{X}$, given by

$${}^\mathcal{X}\boldsymbol{\phi} = \mathcal{Y} \ominus \mathcal{X} \triangleq \mathrm{Log}\left(\mathcal{X}^{-1} \circ \mathcal{Y}\right) \in T_\mathcal{X}\mathcal{M}. \tag{8}$$

Alternatively, a left-invariant formulation can be defined by composing increments on the left-hand side of the group element. In this case, the plus operator is given by Eq. (9).

$$\mathcal{Y} = {}^\mathcal{E}\boldsymbol{\phi} \oplus \mathcal{X} \triangleq \mathrm{Exp}({}^\mathcal{E}\boldsymbol{\phi}) \circ \mathcal{X}, \tag{9}$$

And the corresponding minus operator is

$${}^\mathcal{E}\boldsymbol{\phi} = \mathcal{Y} \ominus \mathcal{X} \triangleq \mathrm{Log}\left(\mathcal{Y} \circ \mathcal{X}^{-1}\right) \in T_\mathcal{E}\mathcal{M}. \tag{10}$$

Both left- and right-invariant definitions provide valid mappings between the Lie group and its tangent spaces. The difference lies in the frame in which the tangent-space quantities are expressed and affects how derivatives and Jacobians are defined. While either formulation may be used, a single convention must be chosen and applied consistently.

2.3 Error-State Kalman Filtering

Inertial navigation estimates the motion of a platform by integrating measurements from an IMU, consisting of accelerometers and gyroscopes. These sensors provide high-rate measurements of specific force and angular velocity, which can be used to propagate position, velocity, and orientation over time. Due to sensor noise and biases, pure inertial integration leads to unbounded drift [11]. To account for uncertainty and allow correction using external measurements, the inertial navigation equations are embedded in a probabilistic filtering framework.

In this work, the inertial navigation equations define the nonlinear motion model of the system. State estimation is performed using an Error-State Kalman Filter, which separates the state into a nominal component that evolves nonlinearly and a small error component evolving in a vector space. This structure is well-suited for systems involving orientations and poses represented on Lie groups [10, 12].

2.3.1 State and Motion Model

The continuous-time IMU and motion model follow the formulations in [10, 11, 13], but attitude is instead represented in SO(3) instead of the Hamiltonian quaternion (S^3). The true state of the system is defined as

$$\mathbf{x_t} = \big(\mathbf{p_t}, \mathbf{v_t}, \mathbf{a}_{bt}, \mathbf{R_t}, \boldsymbol{\omega}_{bt}\big), \tag{11}$$

where $\mathbf{p}_t \in \mathbb{R}^3$ is position, $\mathbf{v}_t \in \mathbb{R}^3$ is velocity, $\mathbf{R}_t \in \mathrm{SO}(3)$ is orientation, and $\mathbf{a}_{bt}, \boldsymbol{\omega}_{bt} \in \mathbb{R}^3$ are the accelerometer and gyroscope biases, respectively. All quantities except for the biases are expressed in a navigation frame unless stated otherwise.

The IMU provides measurements of specific force and angular rate according to

$$\tilde{\mathbf{a}} = \mathbf{R}_t^\top (\dot{\mathbf{v}}_t - \mathbf{g}) + \mathbf{a}_{bt} + \mathbf{a}_n, \qquad \tilde{\boldsymbol{\omega}} = \boldsymbol{\omega}_t + \boldsymbol{\omega}_{bt} + \boldsymbol{\omega}_n, \tag{12}$$

where $\dot{\mathbf{v}}_t$ is the true linear acceleration of the IMU expressed in the navigation frame, and $\mathbf{R}_t^\top (\dot{\mathbf{v}}_t - \mathbf{g})$ is the true specific force expressed in the body frame. The vector $\mathbf{g}$ denotes the local gravity vector and is assumed known. Furthermore, $\mathbf{a}_n$ and $\boldsymbol{\omega}_n$ are zero-mean white measurement noise processes.

The true state is modeled by the continuous-time inertial navigation equations

$$\dot{\mathbf{p}}_t = \mathbf{v}_t, \tag{13}$$

$$\dot{\mathbf{v}}_t = \mathbf{R}_t(\tilde{\mathbf{a}} - \mathbf{a}_{bt} - \mathbf{a}_n) + \mathbf{g}, \tag{14}$$

$$\dot{\mathbf{R}}_t = \mathbf{R}_t\big(\tilde{\boldsymbol{\omega}} - \boldsymbol{\omega}_{bt} - \boldsymbol{\omega}_n\big)^\wedge, \tag{15}$$

$$\dot{\mathbf{a}}_{bt} = -p_{\mathbf{a}b}\,\mathbf{a}_{bt} + \mathbf{a}_w, \tag{16}$$

$$\dot{\boldsymbol{\omega}}_{bt} = -p_{\boldsymbol{\omega}b}\,\boldsymbol{\omega}_{bt} + \boldsymbol{\omega}_w, \tag{17}$$

where $p_{\mathbf{a}b}$ and $p_{\boldsymbol{\omega}b}$ are the inverse time constants of the first-order bias models, and $\mathbf{a}_w \sim \mathcal{N}(\mathbf{0}, \mathbf{Q}_a)$ and $\boldsymbol{\omega}_w \sim \mathcal{N}(\mathbf{0}, \mathbf{Q}_\omega)$ are zero-mean Gaussian white noise processes driving the bias dynamics [13]. In the absence of noise and perturbations, the nominal state coincides with the true state [11]. The nominal state is given by

$$\dot{\mathbf{p}} = \mathbf{v}, \tag{18}$$

$$\dot{\mathbf{v}} = \mathbf{R}(\tilde{\mathbf{a}} - \mathbf{a}_b) + \mathbf{g}, \tag{19}$$

$$\dot{\mathbf{R}} = \mathbf{R}\big(\tilde{\boldsymbol{\omega}} - \boldsymbol{\omega}_b\big)^\wedge, \tag{20}$$

$$\dot{\mathbf{a}}_b = -p_{\mathbf{a}b}\,\mathbf{a}_b, \tag{21}$$

$$\dot{\boldsymbol{\omega}}_b = -p_{\boldsymbol{\omega}b}\,\boldsymbol{\omega}_b, \tag{22}$$

and denoted without the subscript $(\cdot)_t$.

2.3.2 Error-State Definition

Instead of estimating the full state directly, the ESKF maintains an additional state that represents the deviation between the true state and the nominal state. This *error state* is defined in a vector space as

$$\delta\mathbf{x} = \big(\delta\mathbf{p}, \delta\mathbf{v}, \delta\mathbf{a}_b, \delta\boldsymbol{\theta}, \delta\boldsymbol{\omega}_b\big), \tag{23}$$

where $\delta\boldsymbol{\theta} \in \mathbb{R}^3$ denotes a small orientation difference expressed in the tangent space of SO(3), as discussed in Sec. 2.2.2.

The error state relates the true state to the nominal state by

$$\mathbf{x}_t = \mathbf{x} \oplus \delta\mathbf{x} \tag{24}$$

which is the plus operator introduced in Sec. 2.2. In particular, the rotational component satisfies

$$\mathbf{R}_t = \mathbf{R} \oplus \delta\boldsymbol{\theta} = \mathbf{R}\,\mathrm{Exp}(\delta\boldsymbol{\theta}), \tag{25}$$

while the remaining components are related through standard addition. Furthermore, assuming that the error states are small, the following approximations are adopted:

$$\mathrm{Exp}(\delta\boldsymbol{\theta}) = \mathbf{I} + [\delta\boldsymbol{\theta}]_\times + O\big(\|\delta\boldsymbol{\theta}\|^2\big) \ \approx \ \mathbf{I} + [\delta\boldsymbol{\theta}]_\times, \tag{26}$$

$$\delta\mathbf{x}_a \cdot \delta\mathbf{x}_b = O(\|\delta\mathbf{x}_a\|\,\|\delta\mathbf{x}_b\|) \ \approx \ \mathbf{0}, \tag{27}$$

where the first expression corresponds to the small-signal approximation of the exponential map [11], and the second expression reflects the neglect of second-order terms arising from products of small error states, which in this case are $\delta\mathbf{x}_a$ and $\delta\mathbf{x}_b$. Under these assumptions, the error dynamics are linearized to first order.

2.3.3 Error-State Dynamics

By linearizing the inertial navigation equations (18)–(20) around the nominal trajectory, the error-state dynamics can be written in continuous time as

$$\delta\dot{\mathbf{x}} = \mathbf{F}\,\delta\mathbf{x} + \mathbf{G}\,\mathbf{n}, \tag{28}$$

where $\mathbf{F}$ is the error-state Jacobian, $\mathbf{G}$ is the noise input matrix, and $\mathbf{n} \sim \mathcal{N}(\mathbf{0}, \mathbf{Q})$ is the IMU measurement noise and bias process noise. $\mathbf{F}$ and $\mathbf{G}$ can be found in [11] or [13].

The associated error covariance $\mathbf{P}$ evolves according to

$$\dot{\mathbf{P}} = \mathbf{F}\mathbf{P}\mathbf{F}^\top + \mathbf{G}\mathbf{Q}\mathbf{G}^\top, \tag{29}$$

where $\mathbf{Q}$ denotes the continuous-time noise covariance matrix.

2.3.4 Correction and Reset

A filter, as explained above, will inevitably drift over time. If there is a sensor that can give information about the state written as

$$\mathbf{y} = \mathbf{h}(\mathbf{x}_t) + \mathbf{w}, \quad \mathbf{w} \sim \mathcal{N}(\mathbf{0}, \mathbf{V}), \tag{30}$$

where $\mathbf{y}$ is the measurement with noise $\mathbf{w}$, and $\mathbf{h}(\cdot)$ is the measurement prediction function.

Linearizing the measurement model around the nominal state yields the standard ESKF correction equations

$$\mathbf{K} = \mathbf{P}\mathbf{H}^\top(\mathbf{H}\mathbf{P}\mathbf{H}^\top + \mathbf{V})^{-1}, \tag{31}$$

$$\delta\hat{\mathbf{x}} = \mathbf{K}\big(\mathbf{y} - \mathbf{h}(\mathbf{x})\big), \tag{32}$$

$$\mathbf{P} \leftarrow (\mathbf{I} - \mathbf{K}\mathbf{H})\mathbf{P}(\mathbf{I} - \mathbf{K}\mathbf{H})^\top + \mathbf{K}\mathbf{V}\mathbf{K}^\top, \tag{33}$$

where $\delta\hat{\mathbf{x}}$ denotes the estimated mean of the error state, and $\mathbf{H}$ is the Jacobian of the measurement prediction function with respect to the error state, given by

$$\mathbf{H} = \left.\frac{\partial\mathbf{h}(\mathbf{x}\oplus\delta\mathbf{x})}{\partial\delta\mathbf{x}}\right|_{\delta\mathbf{x}=0}. \tag{34}$$

The estimated error-state mean is then injected into the nominal state via

$$\mathbf{x} \leftarrow \mathbf{x}\oplus\delta\hat{\mathbf{x}}. \tag{35}$$

After the injection step, the error state must be redefined such that the nominal state again represents the mean of the state distribution. This is achieved using the error reset mapping

$$\delta\mathbf{x} \leftarrow d(\delta\mathbf{x}) = \delta\mathbf{x}\ominus\delta\hat{\mathbf{x}}, \tag{36}$$

where $\ominus$ is the right-invariant minus operator defined in Sec. 2.2.3. The ESKF error reset operation is thus

$$\delta\hat{\mathbf{x}} \leftarrow \mathbf{0}, \tag{37}$$

$$\mathbf{P} \leftarrow \mathbf{D}\mathbf{P}\mathbf{D}^\top, \tag{38}$$

where $\mathbf{D}$ is the Jacobian of the reset mapping,

$$\mathbf{D} \triangleq \left.\frac{\partial d(\delta\mathbf{x})}{\partial\delta\mathbf{x}}\right|_{\delta\mathbf{x}=\delta\hat{\mathbf{x}}}. \tag{39}$$

3 Method

3.1 System Overview

The implemented estimator follows the ESKF formulation introduced in Sec. 2.3. The inertial navigation equations in Eqs. (18)–(22) define the nonlinear motion model, while the FMCW radar provide radial speed aiding measurements as described in Sec. 2.3.4.

The system uses an IMU from VectorNav, the VN-100 [14], and an FMCW radar from Texas Instruments, the IWR6843AOPEVM [15]. The IMU runs at a higher sampling rate and drives the propagation of the nominal state, whereas radar updates are applied whenever new detections are available. Rotations are represented on SO(3) and updated using the Lie-group tools introduced in Sec. 2.2.

3.1.1 Frame-Explicit State Definition

Throughout this chapter, $_\mathrm{W}\mathbf{p}_\mathrm{WI}$, $_\mathrm{W}\mathbf{v}_\mathrm{WI}$, and $_\mathrm{W}\mathbf{R}_\mathrm{I}$ denote the platform position, velocity, and orientation, respectively, in world frame, while $_I\mathbf{a}_b$ and $_I\boldsymbol{\omega}_b$ denote the accelerometer and gyroscope biases in IMU frame. IMU measurements are also expressed in the IMU frame where $_I\tilde{\mathbf{a}}_\mathrm{WI}$ is the measured specific force, and the measured angular rate is $_I\tilde{\boldsymbol{\omega}}_\mathrm{WI}$. Finally, the states $_I\mathbf{p}_\mathrm{IR}$ and $_\mathrm{R}\mathbf{R}_\mathrm{I}$ denote the radar position and attitude, respectively, expressed in the IMU frame.

Unsubscripted variables denote nominal quantities, the same variables with subscript $(\cdot)_t$ denote the corresponding true quantities, and the associated error-state components are denoted by a prefixed $\delta(\cdot)$. Under this convention, the true state is related to the nominal state by Eq. (24). For completeness, the nominal state is given by

$$\mathbf{x} = \left(_\mathrm{W}\mathbf{p}_\mathrm{WI},\ _\mathrm{W}\mathbf{v}_\mathrm{WI},\ _I\mathbf{a}_b,\ _\mathrm{W}\mathbf{R}_\mathrm{I},\ _I\boldsymbol{\omega}_b,\ _I\mathbf{p}_\mathrm{IR},\ _I\mathbf{R}_\mathrm{R}\right) \tag{40}$$

3.1.2 Radar Measurement Extraction

The radar firmware provides a list of detections for each measurement cycle. Each detection contains a 3D point and its corresponding radial velocity. These quantities correspond to the radar measurement principles presented in Sec. 2.1. The chirp signal that was used is shown in Appendix A. No additional signal-level processing is implemented in this work; the firmware outputs are used directly as radar point clouds.

3.2 Radar Measurement Model

3.2.1 Measurement Prediction Function

Assuming a static environment, the relationship between the linear velocity and the radial speed from the detected point is shown in Fig. 3. From this, it follows that the radial speed corresponds to the projection of the platform's linear velocity onto the line-of-sight unit vector. The sign of the measured radial velocity follows the Doppler convention, where motion towards the radar yields positive values and motion away from the radar yields negative values. This relation can be formulated as

$$v_r = -_\mathrm{R}\boldsymbol{\mu}^\top {}_\mathrm{R}\mathbf{v}_\mathrm{WR} = -_\mathrm{R}\boldsymbol{\mu}^\top {}_\mathrm{R}\mathbf{R}_\mathrm{I}(_\mathrm{W}\mathbf{R}_\mathrm{I}^\top {}_\mathrm{W}\mathbf{v}_\mathrm{WI} + (_I\tilde{\boldsymbol{\omega}}_\mathrm{WI} - {}_I\boldsymbol{\omega}_b) \times {}_I\mathbf{p}_\mathrm{IR}) \tag{41}$$

Where $v_r(\mathbf{x}) = h(\mathbf{x})$ is the measurement prediction function for the radar radial speed, and $-_\mathrm{R}\boldsymbol{\mu}$ denotes the radar line-of-sight (bearing) unit vector pointing from the radar toward the detected target.
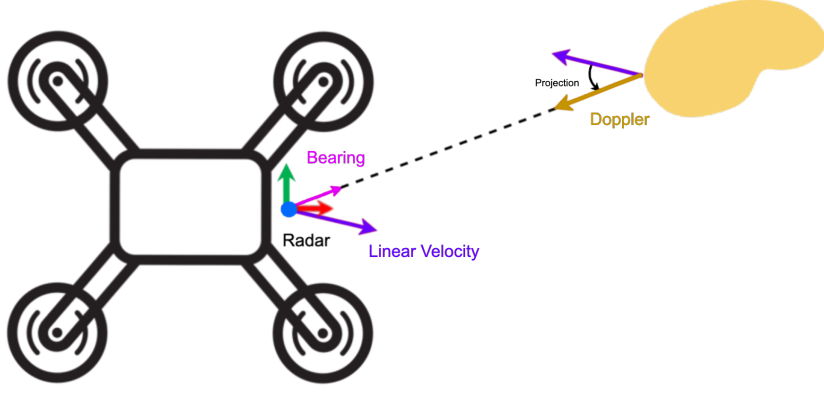
Figure 3: Relationship between the radial speed and the linear velocity, figure inspired by [3].

3.2.2 Derivation of Radar Jacobian

To incorporate the radar measurements into the ESKF, the measurement model in Eq. (41) is linearized with respect to the error state $\delta\mathbf{x}$ defined in Eq. (23), extended to include the radar extrinsic parameters. The Jacobian of the measurement prediction function is given by Eq. (34). We start by writing

$$
\begin{aligned}
\mathbf{h}(\mathbf{x} \oplus \delta\mathbf{x}) = -_\mathrm{R}\boldsymbol{\mu}^\top \big({}_\mathrm{I}\mathbf{R}_\mathrm{R} \oplus \delta\boldsymbol{\theta}_\mathrm{IR}\big)^\top \Big(\big({}_\mathrm{W}\mathbf{R}_\mathrm{I} \oplus \delta\boldsymbol{\theta}_\mathrm{WI}\big)^\top \big({}_\mathrm{W}\mathbf{v}_\mathrm{WI} + \delta_\mathrm{W}\mathbf{v}_\mathrm{WI}\big) \\
+ \big({}_\mathrm{I}\tilde{\boldsymbol{\omega}}_\mathrm{WI} - ({}_\mathrm{I}\boldsymbol{\omega}_b + \delta_\mathrm{I}\boldsymbol{\omega}_b)\big) \times \big({}_\mathrm{I}\mathbf{p}_\mathrm{IR} + \delta_\mathrm{I}\mathbf{p}_\mathrm{IR}\big) \Big)
\end{aligned}
\tag{42}
$$

Applying the definition of the $\oplus$ operator on SO(3) from Eq. (25) to the rotation terms yields

$$
\begin{aligned}
\mathbf{h}(\mathbf{x} \oplus \delta\mathbf{x}) = -_\mathrm{R}\boldsymbol{\mu}^\top \big({}_\mathrm{I}\mathbf{R}_\mathrm{R} \,\mathrm{Exp}(\delta\boldsymbol{\theta}_\mathrm{IR})\big)^\top \Big(\big({}_\mathrm{W}\mathbf{R}_\mathrm{I} \,\mathrm{Exp}(\delta\boldsymbol{\theta}_\mathrm{WI})\big)^\top \big({}_\mathrm{W}\mathbf{v}_\mathrm{WI} + \delta_\mathrm{W}\mathbf{v}_\mathrm{WI}\big) \\
+ \big({}_\mathrm{I}\tilde{\boldsymbol{\omega}}_\mathrm{WI} - ({}_\mathrm{I}\boldsymbol{\omega}_b + \delta_\mathrm{I}\boldsymbol{\omega}_b)\big) \times \big({}_\mathrm{I}\mathbf{p}_\mathrm{IR} + \delta_\mathrm{I}\mathbf{p}_\mathrm{IR}\big) \Big)
\end{aligned}
\tag{43}
$$

Using the small-signal assumption in Eq. (26), we can approximate Eq. (43) as

$$
\begin{aligned}
\mathbf{h}(\mathbf{x} \oplus \delta\mathbf{x}) \approx -\boldsymbol{\mu}^\top ({}_\mathrm{I}\mathbf{R}_\mathrm{R}(\mathbf{I} + [\delta\boldsymbol{\theta}_\mathrm{IR}]))^\top \cdot \\
\Big((\mathbf{R}(\mathbf{I} + [\delta\boldsymbol{\theta}]))^\top (\mathbf{v} + \delta\mathbf{v}) + (\tilde{\boldsymbol{\omega}} - (\boldsymbol{\omega}_b + \delta\boldsymbol{\omega}_b)) \times ({}_\mathrm{I}\mathbf{p}_\mathrm{IR} + \delta_\mathrm{I}\mathbf{p}_\mathrm{IR}) \Big)
\end{aligned}
\tag{44}
$$

where subscripts denoting reference frames are omitted for simplicity, except for the radar extrinsics. Expanding the expression and neglecting second-order error terms yields

$$
\begin{aligned}
\mathbf{h}(\mathbf{x} \oplus \delta\mathbf{x}) \approx -\boldsymbol{\mu}^\top \Big({}_\mathrm{R}\mathbf{R}_\mathrm{I}(\mathbf{R}^\top\mathbf{v} + \mathbf{R}^\top\delta\mathbf{v} - [\delta\boldsymbol{\theta}]\mathbf{R}^\top\mathbf{v} + [\tilde{\boldsymbol{\omega}}]_\times {}_\mathrm{I}\mathbf{p}_\mathrm{IR} \\
+ [\tilde{\boldsymbol{\omega}}]_\times \delta_\mathrm{I}\mathbf{p}_\mathrm{IR} - [\boldsymbol{\omega}_b]_\times {}_\mathrm{I}\mathbf{p}_\mathrm{IR} - [\delta\boldsymbol{\omega}_b]_\times {}_\mathrm{I}\mathbf{p}_\mathrm{IR} - [\boldsymbol{\omega}_b]_\times \delta_\mathrm{I}\mathbf{p}_\mathrm{IR}) \\
+ [\delta\boldsymbol{\theta}_\mathrm{IR}]^\top ({}_\mathrm{I}\mathbf{R}_\mathrm{R}^\top \mathbf{R}^\top\mathbf{v} + {}_\mathrm{I}\mathbf{R}_\mathrm{R}^\top [\tilde{\boldsymbol{\omega}}]_\times {}_\mathrm{I}\mathbf{p}_\mathrm{IR} - {}_\mathrm{I}\mathbf{R}_\mathrm{R}^\top [\boldsymbol{\omega}_b]_\times {}_\mathrm{I}\mathbf{p}_\mathrm{IR}) \Big)
\end{aligned}
\tag{45}
$$

By using that the vector cross product is anti-commutative, satisfying $\mathbf{a} \times \mathbf{b} = -\mathbf{b} \times \mathbf{a}$, following [16], and that the transpose of a skew-symmetric matrix can be written as $[\mathbf{a}]_\times^\top = -[\mathbf{a}]_\times$, the

non-zero elements of the Jacobian for the radar radial speed can be written as

$$\frac{\partial \mathbf{h}(\mathbf{x} \oplus \delta \mathbf{x})}{\partial \delta_{\mathrm{W}} \mathbf{v}_{\mathrm{WI}}} = \mathbf{H}_{\delta_{\mathrm{W}} \mathbf{v}_{\mathrm{WI}}} = -_{\mathrm{R}} \boldsymbol{\mu}^{\top}{}_{\mathrm{R}} \mathbf{R}_{\mathrm{IW}} \mathbf{R}_{\mathrm{I}}^{\top} \tag{46}$$

$$\frac{\partial \mathbf{h}(\mathbf{x} \oplus \delta \mathbf{x})}{\partial \delta \boldsymbol{\theta}_{\mathrm{WI}}} = \mathbf{H}_{\delta \boldsymbol{\theta}_{\mathrm{WI}}} = -_{\mathrm{R}} \boldsymbol{\mu}^{\top}{}_{\mathrm{R}} \mathbf{R}_{\mathrm{I}} [_{\mathrm{W}} \mathbf{R}_{\mathrm{I}}^{\top} {}_{\mathrm{W}} \mathbf{v}_{\mathrm{WI}}]_{\times} \tag{47}$$

$$\frac{\partial \mathbf{h}(\mathbf{x} \oplus \delta \mathbf{x})}{\partial \delta_{\mathrm{I}} \boldsymbol{\omega}_b} = \mathbf{H}_{\delta_{\mathrm{I}} \boldsymbol{\omega}_b} = -_{\mathrm{R}} \boldsymbol{\mu}^{\top}{}_{\mathrm{R}} \mathbf{R}_{\mathrm{I}} [_{\mathrm{I}} \mathbf{p}_{\mathrm{IR}}]_{\times} \tag{48}$$

$$\frac{\partial \mathbf{h}(\mathbf{x} \oplus \delta \mathbf{x})}{\partial \delta_{\mathrm{I}} \mathbf{p}_{\mathrm{IR}}} = \mathbf{H}_{\delta_{\mathrm{I}} \mathbf{p}_{\mathrm{IR}}} = -_{\mathrm{R}} \boldsymbol{\mu}^{\top}{}_{\mathrm{R}} \mathbf{R}_{\mathrm{I}} [_{\mathrm{I}} \tilde{\boldsymbol{\omega}}_{\mathrm{WI}} - {}_{\mathrm{I}} \boldsymbol{\omega}_b]_{\times} \tag{49}$$

$$\frac{\partial \mathbf{h}(\mathbf{x} \oplus \delta \mathbf{x})}{\partial \delta \boldsymbol{\theta}_{\mathrm{IR}}} = \mathbf{H}_{\delta \boldsymbol{\theta}_{\mathrm{IR}}} = -_{\mathrm{R}} \boldsymbol{\mu}^{\top} [_{\mathrm{I}} \mathbf{R}_{\mathrm{R}}^{\top} (_{\mathrm{W}} \mathbf{R}_{\mathrm{I}}^{\top} {}_{\mathrm{W}} \mathbf{v}_{\mathrm{WI}} + [_{\mathrm{I}} \tilde{\boldsymbol{\omega}}_{\mathrm{WI}} - {}_{\mathrm{I}} \boldsymbol{\omega}_b]_{\times} {}_{\mathrm{I}} \mathbf{p}_{\mathrm{IR}})]_{\times} \tag{50}$$

The complete analytic Jacobian $\mathbf{H}$ is assembled by placing the individual blocks in the appropriate locations corresponding to the ordering of the error-state vector, and is written as

$$\mathbf{H} = \begin{bmatrix} \mathbf{0}_{1 \times 3} & \mathbf{H}_{\delta_{\mathrm{W}} \mathbf{v}_{\mathrm{WI}}} & \mathbf{0}_{1 \times 3} & \mathbf{H}_{\delta \boldsymbol{\theta}_{\mathrm{WI}}} & \mathbf{H}_{\delta_{\mathrm{I}} \boldsymbol{\omega}_b} & \mathbf{H}_{\delta_{\mathrm{I}} \mathbf{p}_{\mathrm{IR}}} & \mathbf{H}_{\delta \boldsymbol{\theta}_{\mathrm{IR}}} \end{bmatrix}, \tag{51}$$

Numerical Validation   The analytical Jacobian was validated by comparison with a numerical Jacobian obtained using a central-difference approximation of the measurement prediction function in Eq. (30). Starting from the nominal state, each component of the error-state vector was independently perturbed by a small increment $\delta \boldsymbol{x}_k$, while all other components were held fixed. The perturbations were applied using the same error-state mapping assumed in the analytical derivation in Eq. (34).

For each error-state component k, the corresponding column of the numerical Jacobian was computed as

$$\mathbf{H}_k \approx \frac{h(\boldsymbol{x} \oplus \delta \boldsymbol{x}_k) - h(\boldsymbol{x} \oplus (-\delta \boldsymbol{x}_k))}{2 \|\delta \boldsymbol{x}_k\|}, \tag{52}$$

where $\delta \boldsymbol{x}_k$ is a perturbation applied along the k-th error-state direction.

The resulting numerical Jacobian was compared against the analytical Jacobian, and the norm of their difference was evaluated for each error-state block. Table 1 summarizes the results and shows that the error is sufficiently small for a range of perturbations.

Table 1: Block-wise central-difference of non-zero Jacobian error $\|\Delta \mathbf{H}\|_2 = \|\mathbf{H}_{\mathrm{numerical}} - \mathbf{H}_{\mathrm{analytical}}\|_2$ for decreasing step size $\delta \mathbf{x}$.

$\delta \mathbf{x}$	$\| \Delta \mathbf{H}_{\delta_{\mathrm{W}} \mathbf{v}_{\mathrm{WI}}} \|_2$	$\| \Delta \mathbf{H}_{\delta \boldsymbol{\theta}_{\mathrm{WI}}} \|_2$	$\| \Delta \mathbf{H}_{\delta_{\mathrm{I}} \boldsymbol{\omega}_b} \|_2$	$\| \Delta \mathbf{H}_{\delta_{\mathrm{I}} \mathbf{p}_{\mathrm{IR}}} \|_2$	$\| \Delta \mathbf{H}_{\delta \boldsymbol{\theta}_{\mathrm{IR}}} \|_2$
10^{-2}	1.80×10^{-14}	2.57×10^{-5}	1.50×10^{-14}	1.81×10^{-14}	2.14×10^{-5}
10^{-3}	1.99×10^{-13}	2.57×10^{-7}	1.42×10^{-13}	2.11×10^{-13}	2.14×10^{-7}
10^{-4}	2.61×10^{-12}	2.57×10^{-9}	1.39×10^{-12}	2.80×10^{-12}	2.14×10^{-9}
10^{-5}	1.47×10^{-11}	1.93×10^{-11}	1.10×10^{-11}	1.14×10^{-11}	2.70×10^{-11}

3.3   Error-State Kalman Filter Implementation

This section describes the discrete-time implementation of the Error-State Kalman Filter introduced in Sec. 2.3. The filter maintains a nominal state propagated by IMU integration and an associated error state with covariance capturing local uncertainty.

3.3.1   Discrete-Time Propagation

Let $\Delta t_k = t_k - t_{k-1}$ denote the IMU sampling interval, at discrete timesteps $k = 1, 2, \dots$. The nominal state is propagated by direct integration of the inertial navigation equations (Eqs. (18)–(22)), with attitude updates applied on SO(3) using the exponential map.

The error-state dynamics are obtained by linearizing the continuous-time system dynamics and can be written as

$$\delta\dot{\mathbf{x}}(t) = \mathbf{F}\,\delta\mathbf{x}(t) + \mathbf{G}\,\mathbf{n}(t), \qquad \mathbf{n}(t) \sim \mathcal{N}(\mathbf{0}, \mathbf{Q}), \tag{53}$$

and is given by Eq. (28). Assuming $\mathbf{F}$ and $\mathbf{G}$ are constant over one interval, the zero-order hold (ZOH) discretization [13] is given by

$$\mathbf{\Phi}_k = \exp(\mathbf{F}\Delta t_k). \tag{54}$$

In this work, a first-order approximation of the matrix exponential is used,

$$\mathbf{\Phi}_k \approx \mathbf{I} + \mathbf{F}\Delta t_k, \tag{55}$$

which follows directly from the Taylor expansion of $\exp(\mathbf{F}\Delta t_k)$ and is sufficient at the IMU update rate used.

The discrete process-noise covariance is defined by

$$\mathbf{Q}_{d,k} = \int_0^{t_k} e^{(t_k - \tau)\mathbf{F}}\,\mathbf{G}\mathbf{Q}\mathbf{G}^\top e^{(t_k - \tau)\mathbf{F}^\top}\,\mathrm{d}\tau, \tag{56}$$

which is approximated consistently to first order as

$$\mathbf{Q}_{d,k} \approx \mathbf{G}\mathbf{Q}\mathbf{G}^\top \Delta t_k. \tag{57}$$

The resulting covariance propagation is

$$\mathbf{P}_{k+1} = \mathbf{\Phi}_k \mathbf{P}_k \mathbf{\Phi}_k^\top + \mathbf{Q}_{d,k}. \tag{58}$$

A higher-fidelity discretization can be obtained by computing $\mathbf{\Phi}_k = \exp(\mathbf{F}\Delta t_k)$ and evaluating $\mathbf{Q}_{d,k}$ using Van Loan discretization [13], but this would come at the cost of computational speed.

3.3.2 Radar Measurement Update

Radar updates are applied whenever a new radar point cloud is available. Each detected point provides a radial speed given by

$$y = h(\mathbf{x}_t) + w, \quad w \sim \mathcal{N}(0, \sigma^2) \tag{59}$$

where σ denotes the scalar standard deviation of the radar measurement noise.

Under the static-world assumption, the radial speed measurement is only related to ego-motion. The corresponding measurement prediction function $h(\mathbf{x})$ is given in Eq. (41).

For each detection i at timestep k, a scalar residual is formed,

$$r_{k,i} = y_{k,i} - h(\mathbf{x}_{k,i}), \tag{60}$$

with Jacobian row $\mathbf{H}_{k,i}$ assembled from the analytic expressions derived in Sec. 3.2.2. The innovation variance is

$$S_{k,i} = \mathbf{H}_{k,i}\mathbf{P}_k\mathbf{H}_{k,i}^\top + \sigma^2. \tag{61}$$

Sequential fusion and gating Radar detections are fused sequentially. Before applying an update, each detection is gated using the normalized innovation squared,

$$\gamma_{k,i} = \frac{r_{k,i}^2}{S_{k,i}}. \tag{62}$$

A measurement is accepted if $\gamma_{k,i} \leq \sigma_{gate}^2$, where σ_{gate} is the chosen gating threshold in units of standard deviations [13]. Rejected detections do not affect the state or covariance.

For accepted measurements, the Kalman gain and error-state update are

$$\mathbf{K}_{k,i} = \mathbf{P}_k \mathbf{H}_{k,i}^\top S_{k,i}^{-1}, \qquad \delta\hat{\mathbf{x}}_{k,i} = \mathbf{K}_{k,i} r_{k,i}, \tag{63}$$

and the covariance is updated using the Joseph form,

$$\mathbf{P}_k = (\mathbf{I} - \mathbf{K}_{k,i}\mathbf{H}_{k,i})\mathbf{P}_k(\mathbf{I} - \mathbf{K}_{k,i}\mathbf{H}_{k,i})^\top + \mathbf{K}_{k,i}\,\sigma^2\,\mathbf{K}_{k,i}^\top. \tag{64}$$

After each accepted radar update, the correction is injected into the nominal state, and the filter is reset before processing the next detection.

3.3.3 Injection and Reset

The estimated error state $\delta\hat{\mathbf{x}}$ is injected into the nominal state using the $\oplus$ operator defined in Sec. 2.2. Euclidean components are updated additively, while rotational components are updated on SO(3).

After injection, the error-state mean is reset to zero, as discussed in Sec. 2.3.4. Because orientation errors live in a tangent space, the covariance must be transformed by the reset Jacobian,

$$\delta\hat{\mathbf{x}} \leftarrow \mathbf{0}, \qquad \mathbf{P} \leftarrow \mathbf{D}\mathbf{P}\mathbf{D}^\top, \tag{65}$$

where $\mathbf{D}$ is given in Eq. (39). $\mathbf{D}$ is equal to the identity $\mathbf{I}$ for all states except the rotational states, which are equal to

$$\mathbf{D}_{\delta\boldsymbol{\theta}} = \mathbf{I} - \frac{1}{2}[\delta\hat{\boldsymbol{\theta}}]_\times, \tag{66}$$

3.3.4 Initialization

The filter is initialized under the assumption that the platform is stationary at start-up. The nominal position and velocity are set to zero, and the initial yaw is fixed to zero as a reference heading. Roll and pitch are initialized from the accelerometer by exploiting that the measured specific force is dominated by gravity when the platform is at rest. Concretely, if $\|_{\mathrm{I}}\tilde{\mathbf{a}}_{\mathrm{WI}}\| \approx \|_{\mathrm{W}}\mathbf{g}\|$, the accelerometer vector is used to align the body z-axis with gravity and compute an initial roll–pitch attitude estimate.

All IMU bias states are initialized to zero. The radar extrinsic parameters are initialized from a prior estimate (measured before flight), and are treated as constant in the motion model, but are allowed to adjust through the radial speed measurements by assigning a non-zero prior covariance.

The initial uncertainty is given by a diagonal covariance matrix with standard deviations listed in Table 2. Roll and pitch are given relatively high confidence due to gravity alignment, whereas yaw is initialized with very high confidence (fixed reference). Conservative uncertainty is used for the IMU bias terms and for the radar extrinsics to allow online refinement.

Table 2: Standard deviations used to construct the diagonal prior covariance $\mathbf{P}_0$.

State block	Frame	Std. dev.	Units
Attitude (roll, pitch, yaw)	World	$(6.0,\ 6.0,\ 1.0 \times 10^{-6})$	deg
Position	World	1.0×10^{-6} per axis	m
Velocity	World	1.0×10^{-1} per axis	m/s
Accelerometer bias	IMU	1.0×10^{-2} per axis	m/s^2
Gyroscope bias	IMU	1.0×10^{-4} per axis	rad/s
Radar position	IMU	2.0×10^{-3} per axis	m
Radar attitude (roll, pitch, yaw)	IMU	0.5 per axis	deg

4 Results and Discussion

This section evaluates the performance of the proposed radar-inertial ESKF described in Sec. 3. The estimated trajectories are compared to a LiDAR–inertial odometry (LIO) baseline obtained by using the method from [4] and disabling the radar factors. These trajectories will be used as ground truth where the origin is aligned using the `align_origin` function from [17]. To plot the angles, the XYZ Euler-angle convention was used. The evaluation is conducted on three experimental datasets with distinct motion characteristics:

- **Experiment A (square trajectory):** primarily piecewise planar motion with repeated turns and an extended hover period,

- **Experiment B (random motion):** irregular translational and rotational maneuvers with frequent excitation,

- **Experiment C (circular trajectory):** approximately circular planar motion.

All datasets are processed offline using identical filter parameters, except for the radar radial speed gating threshold, which is varied to assess robustness. Results are shown with $\sigma_{gate} = 3$ if not stated otherwise, and ground truth is used solely for evaluation and is not available to the estimator.

4.1 Trajectory Estimation

Fig. 4 shows the estimated trajectories for all datasets overlaid with ground truth.

Across all datasets, a continuous drift in the vertical (z) direction is observed, shown in Fig. 5. In Experiment C, the vertical estimate exhibits a pronounced divergence during a mid-flight interval shown in Fig. 5c.

There is also a slowly increasing yaw drift in the trajectory. In the radar radial speed update, the gyroscope bias enters the measurement model only through the rigid-body lever-arm term between the IMU and the radar. As shown by the radial speed measurement Jacobian, the sensitivity with respect to the gyroscope bias is proportional to the skew-symmetric matrix of the radar lever arm, given by

$$\frac{\partial h}{\partial \delta_{\mathrm{I}} \boldsymbol{\omega}_b} \propto [_{\mathrm{I}} \mathbf{p}_{\mathrm{IR}}]_\times$$

For short lever arms, this term becomes very small, making the yaw-rate bias only weakly observable through radial speed measurements alone. This limitation has been noted in prior work on radar–inertial odometry, where it is shown that even moderate yaw-rate bias errors induce velocity errors that are typically well below the noise level of low-cost FMCW radar sensors when the lever arm is small [18]. As a result, the yaw-rate bias is weakly observable and difficult to estimate accurately. The resulting yaw drift accumulates over time in all datasets, as seen in Fig. 6.

4.2 Absolute Pose Error

The Absolute Pose Error (APE) measures the deviation between the estimated trajectory and ground truth after alignment. In this work, APE is reported for the translational component only to summarize the growth of position error over time.

Fig. 7 shows the translational APE for all datasets. Among the three datasets, Experiment C exhibits the largest APE, despite maintaining continuous translational and rotational motion. This behavior is primarily driven by the pronounced vertical drift observed in Fig. 5c, which dominates the translational error during a prolonged interval and leads to a rapid increase in APE.
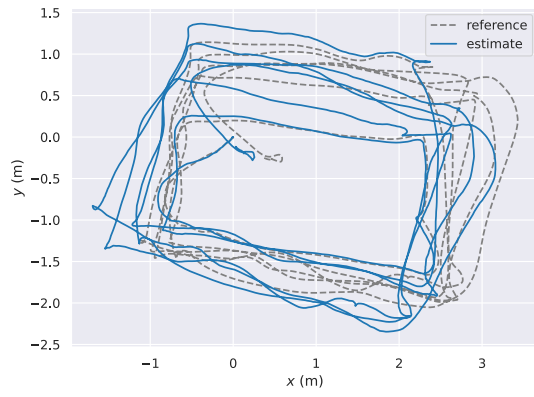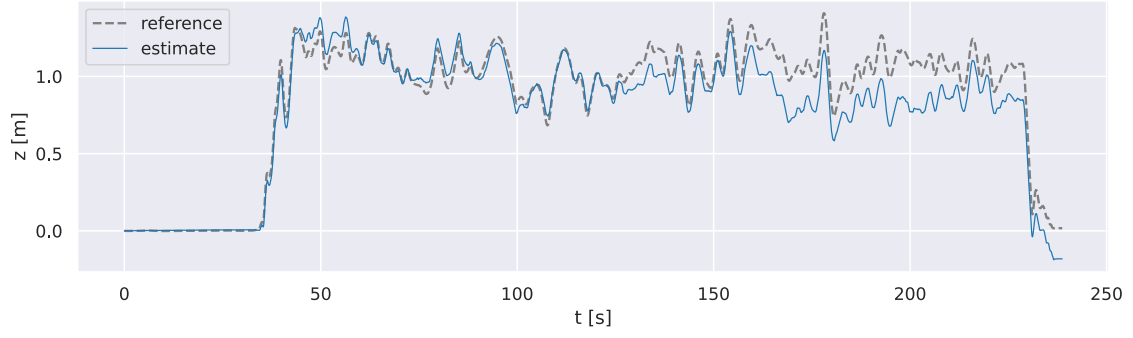
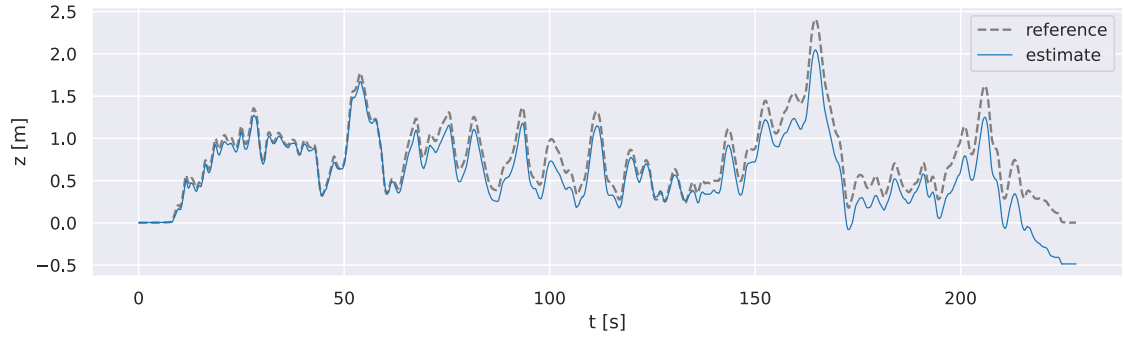(a) Experiment A.
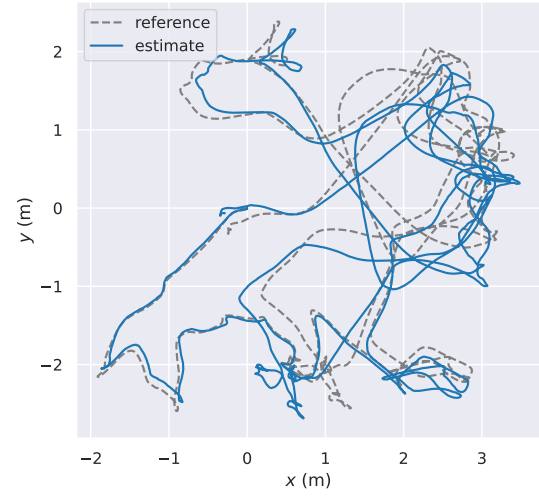
(b) Experiment B.
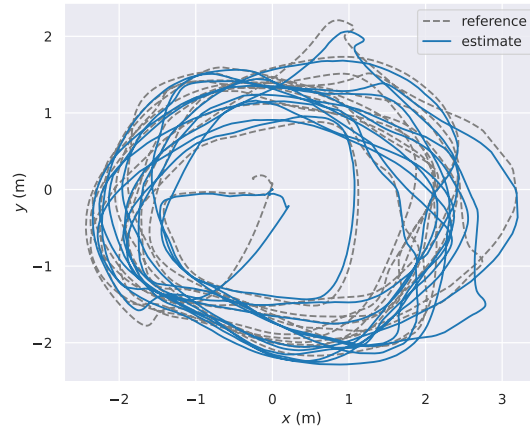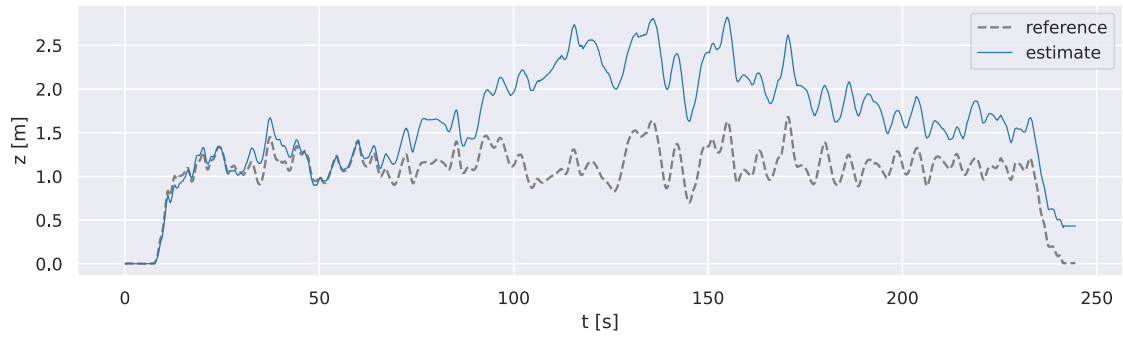

(c) Experiment C.

Figure 4: Estimated trajectories (blue) compared to ground truth (grey).
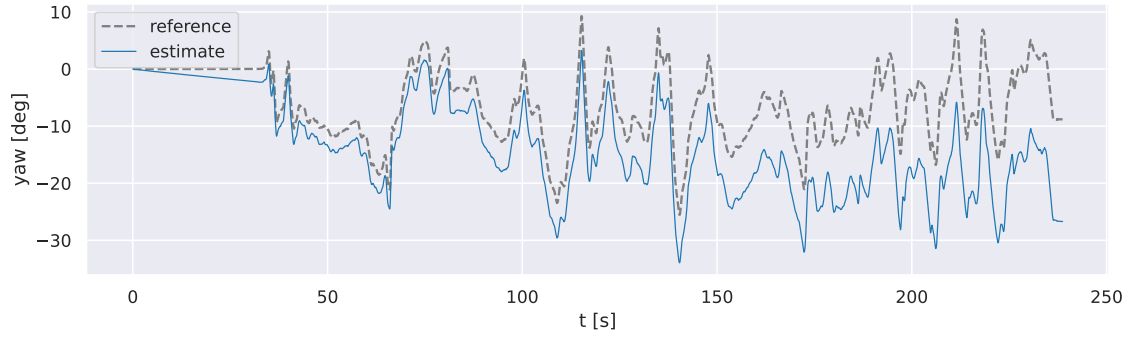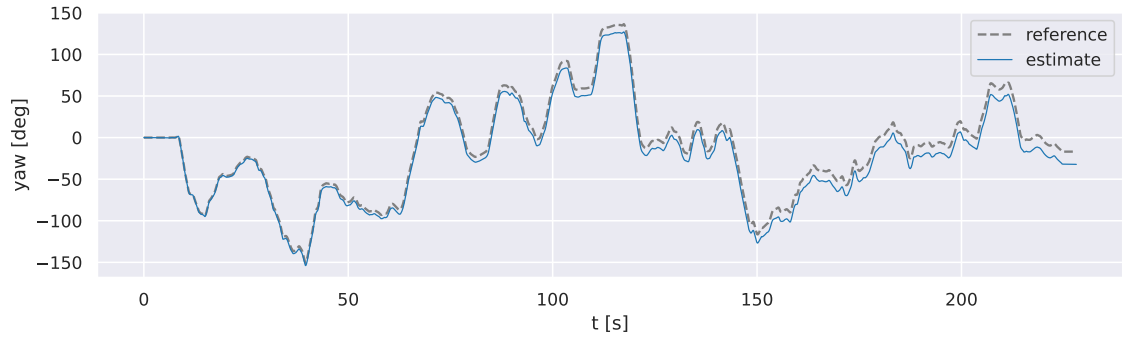
(a) Experiment A.
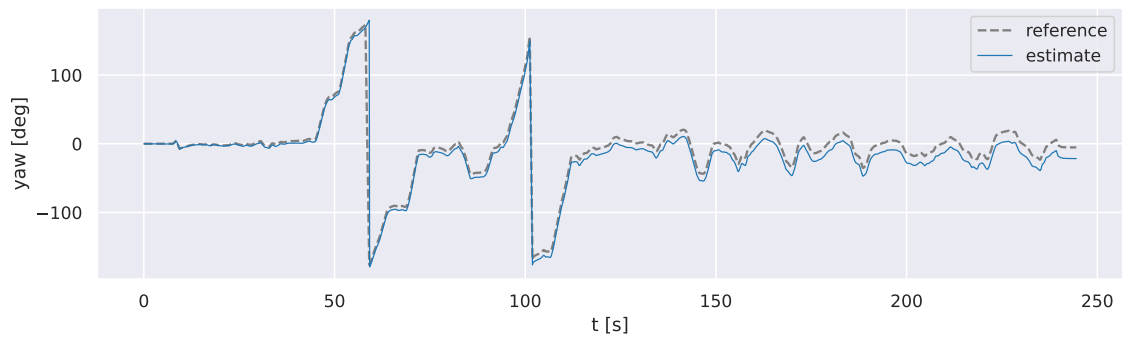

(b) Experiment B.

(c) Experiment C.

Figure 5: Estimated height (blue) compared to ground truth (grey) for all experiments.

(a) Experiment A. Final yaw error: 16.3 deg

(b) Experiment B. Final yaw error: 15.3 deg

(c) Experiment C. Final yaw error: 17.9 deg
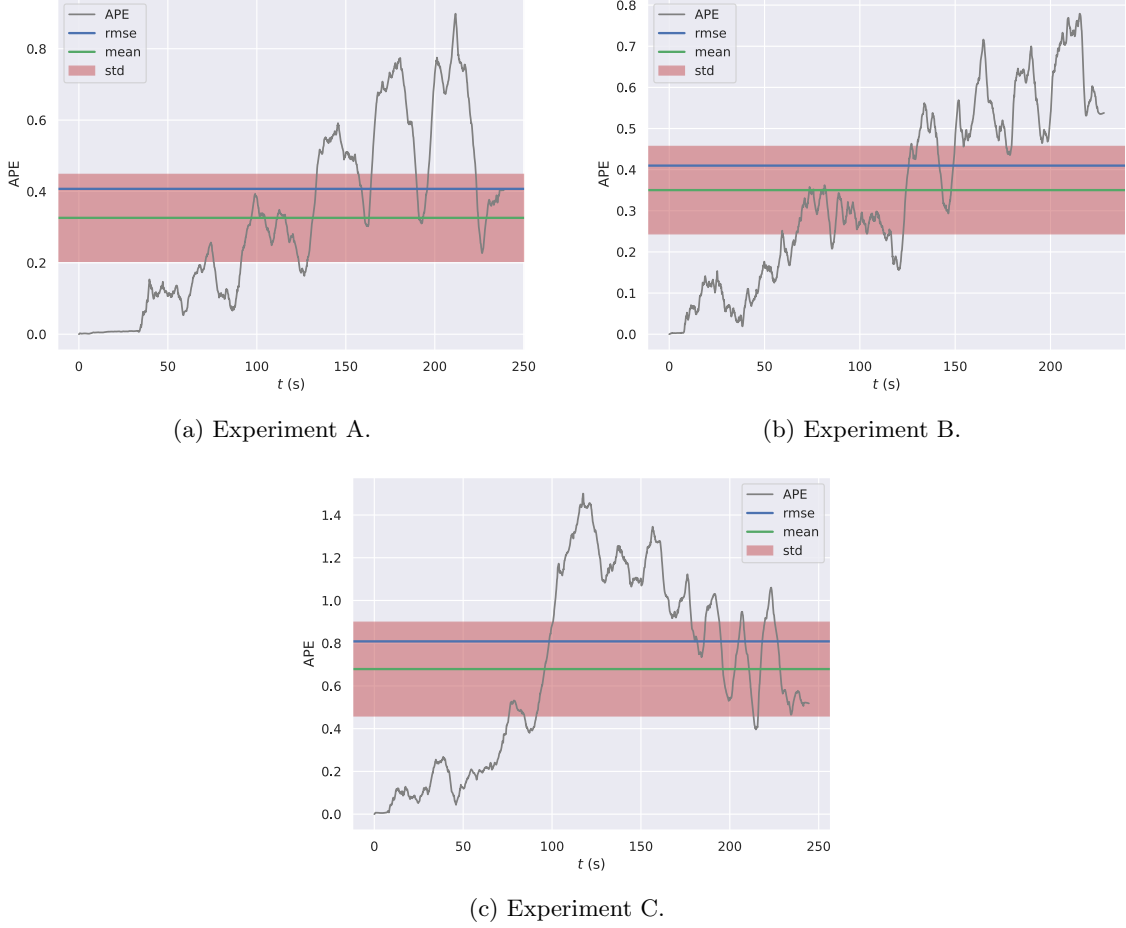
Figure 6: Estimated yaw (blue) compared to ground truth (grey) yaw for all experiments.

(a) Experiment A.

(b) Experiment B.

(c) Experiment C.

Figure 7: Absolute Pose Error over time for all experiments, showing RMSE, mean error, and ± 1 standard deviation.

Experiment A and B show moderate APE growth, with translational error accumulating gradually over time. Since APE is evaluated on translation only, orientation drift contributes to the metric only indirectly through its effect on position propagation.

4.3   Relative Pose Error

RPE evaluates local trajectory consistency over a fixed distance and is independent of global alignment. RPE is well-suited to assess short-term estimator accuracy and dynamic consistency. Fig. 8 shows the RPE for all experiments over all 10m segments.

Across all datasets, RPE remains low and bounded, including for Experiment C. This indicates that even during periods of reduced global observability, the estimator maintains locally consistent motion estimates.

The consistently lower RPE compared to APE indicates that the estimator preserves short-horizon motion consistency even when long-horizon errors accumulate. This is expected because radial speed updates aid velocity, which dominates the relative motion over a fixed 10 m segment, while weakly observable modes (notably z and yaw) primarily affect long-term drift.
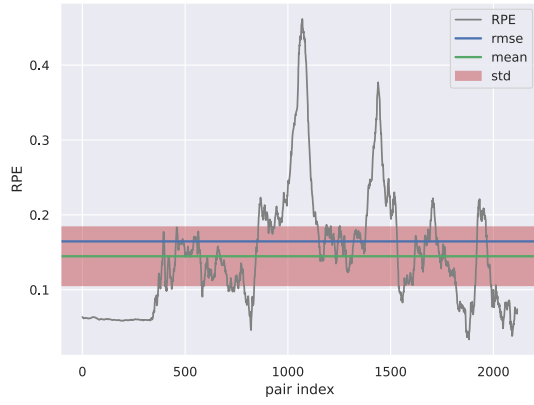
(a) Experiment A.

(b) Experiment B.
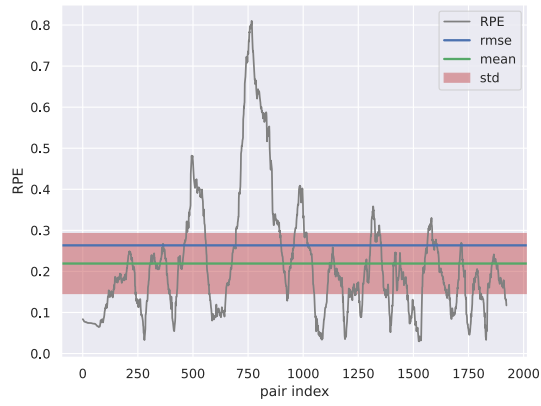
(c) Experiment C.

Figure 8: Relative Pose Error over time for all experiments, showing RMSE, mean error, and $\pm$ 1 standard deviation.

4.4 Quantitative Evaluation

Table 3 and Table 4 summarize translation-only APE and RPE RMSE, respectively, across all datasets for different radar radial speed gating thresholds. The gating parameter σ_{gate} corresponds to the normalized innovation test $\gamma \leq \sigma_{gate}^2$ described in Sec. 3.3.2.

Across all motion patterns, moderate gating values ($\sigma_{gate} = 3$–5) consistently yield the lowest RPE RMSE. Tighter gating ($\sigma_{gate} = 2$) rejects a significant portion of valid radial speed measurements, reducing the information available to the filter, particularly during aggressive maneuvers. Conversely, looser gating ($\sigma_{gate} \geq 8$) allows occasional outliers to enter the update step, slightly degrading estimation accuracy.

The consistency of this trend across all datasets suggests that the gating strategy offers a robust mechanism for balancing measurement reliability and information usage, regardless of the underlying motion pattern.

Table 3: Translation APE RMSE [m] for different radar radial speed gating thresholds σ_{gate}. Values are reported as mean RMSE $\pm$ one standard deviation across runs, in meters.

	Experiment		
Gating (σ_{gate})	A (square)	B (random)	C (circular)
2.0	0.44 ± 0.24	57.29 ± 44.27	0.68 ± 0.37
3.0	0.40 ± 0.24	0.41 ± 0.21	0.81 ± 0.44
4.0	0.49 ± 0.29	0.52 ± 0.25	0.66 ± 0.36
5.0	0.45 ± 0.26	0.53 ± 0.25	0.66 ± 0.37
8.0	0.52 ± 0.32	0.71 ± 0.32	1.23 ± 0.63

Table 4: Translation RPE RMSE [m] for different radar radial speed gating thresholds σ_{gate} (RPE: $\Delta = 10$ m, all_pairs). Values are reported as mean RMSE $\pm$ one standard deviation across runs, in meters.
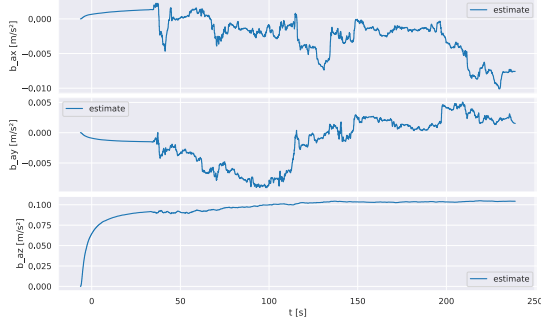
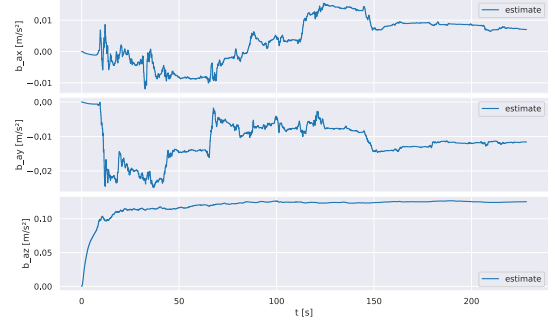|	Experiment		
Gating (σ_{gate})	A (square)	B (random)	C (circular)
2.0	0.21 ± 0.084	4.58 ± 3.52	0.30 ± 0.17
3.0	0.16 ± 0.078	0.17 ± 0.064	0.26 ± 0.15
4.0	0.18 ± 0.080	0.20 ± 0.069	0.24 ± 0.13
5.0	0.19 ± 0.091	0.22 ± 0.079	0.22 ± 0.10
8.0	0.20 ± 0.077	0.26 ± 0.091	0.29 ± 0.13

4.5 State and Parameter Convergence

In addition to trajectory accuracy, the convergence behavior of internal states and parameters provides insight into the consistency and observability of this estimator. Of particular interest are IMU bias estimates and radar extrinsic parameters, which are not directly measured but inferred through their effect on the motion and measurement models.

The estimated accelerometer biases converge rapidly across all datasets, as shown in Fig. 9. This is expected, since accelerometer biases directly affect velocity propagation and are observable through radial speed updates. Gyroscope bias convergence, shown in Fig. 10, is slower.
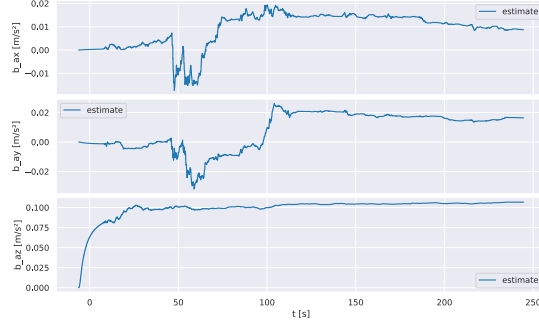
The radar extrinsic parameters (Figs. 11–12) remain bounded and exhibit convergence toward steady values. This indicates that the radial speed measurements provide sufficient excitation for online refinement of the extrinsics, although convergence is slower in Experiment A due to extended low-dynamics periods.
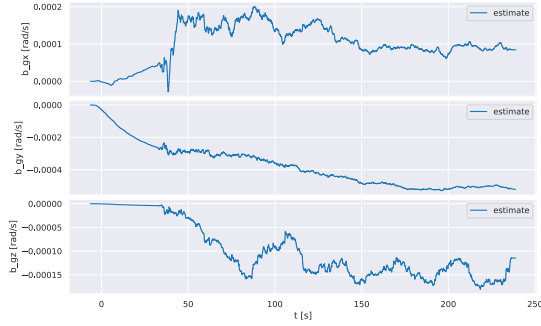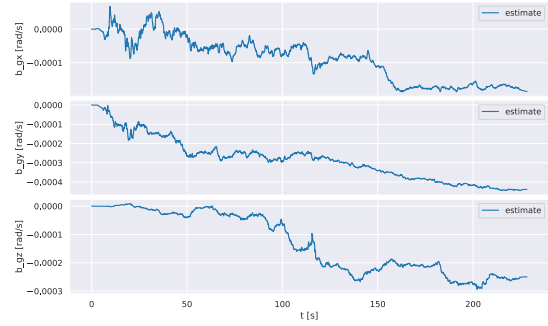
(a) Experiment A.
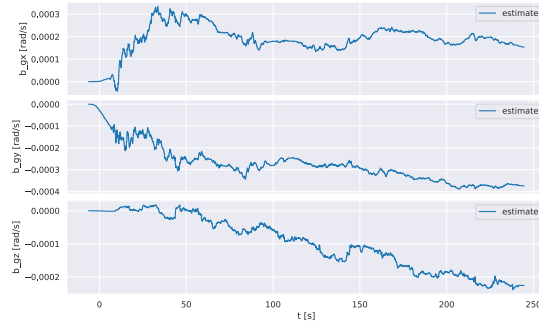
(b) Experiment B.

(c) Experiment C.

Figure 9: Estimated accelerometer bias components over time for all experiments.
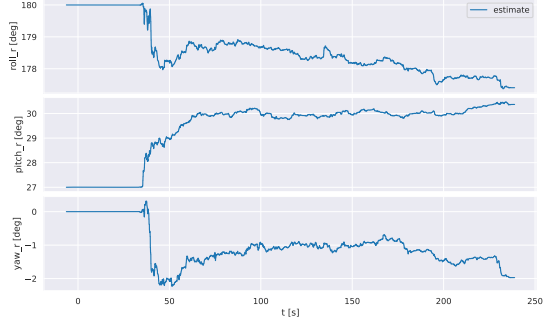

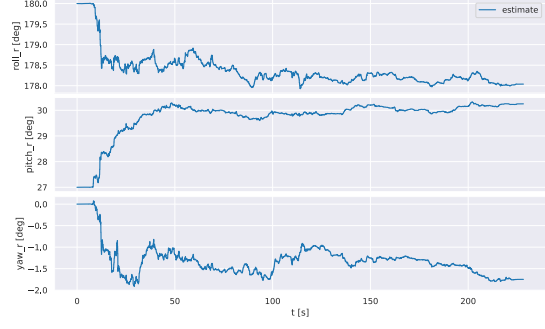(a) Experiment A.
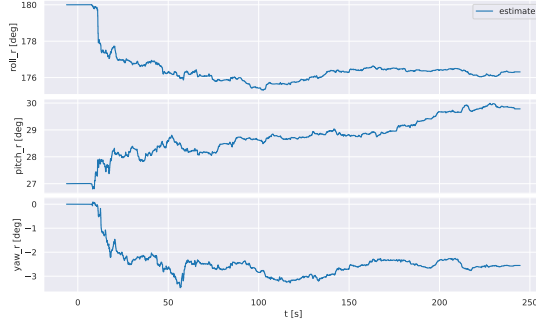
(b) Experiment B.

(c) Experiment C.

Figure 10: Gyroscope bias over time for all experiments.
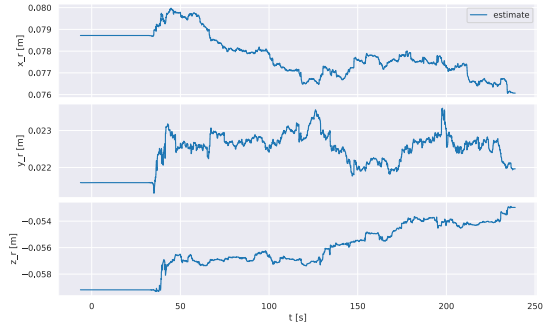
(a) Experiment A.
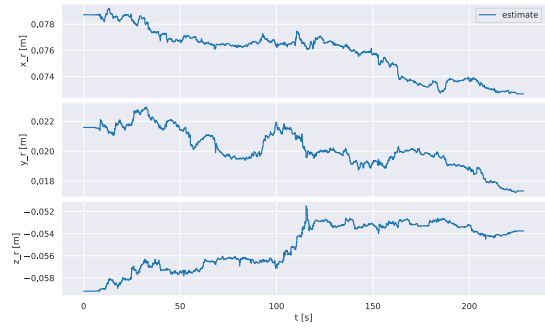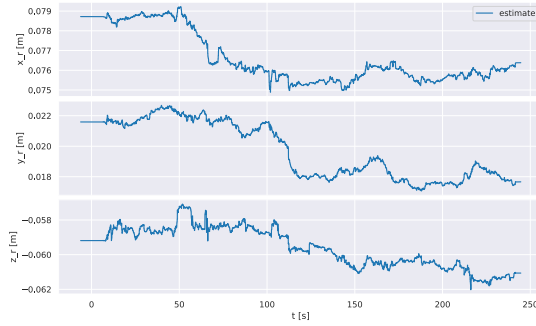
(b) Experiment B.

(c) Experiment C.

Figure 11: Radar attitude over time for all experiments.

(a) Experiment A.

(b) Experiment B.

(c) Experiment C.

Figure 12: Radar position over time for all experiments.

5 Conclusion and Future Work

5.1 Conclusion

This work presented a radar–inertial error-state Kalman filter that fuses IMU measurements with radial speed observations from an FMCW radar. The estimator employs an error-state representation, per-point radial speed measurement aiding, and online estimation of radar extrinsic parameters.

Experimental results on three datasets with different motion profiles show that radar radial speed measurements provide reliable constraints on translational velocity and contribute to stabilizing the yaw estimate when sufficient motion excitation is present. The Relative Pose Error remains low and bounded across all datasets, indicating that the estimator maintains good local consistency over short time horizons.

At the same time, the results highlight limitations of the proposed formulation. All datasets exhibit drift in the vertical direction, and yaw drift occurs during periods of low translational excitation. The Absolute Pose Error, evaluated on the translational component, increases over time and is most pronounced for the circular trajectory dataset, where vertical drift dominates.

The results show that radar radial speed measurements are effective for maintaining short-term inertial navigation accuracy. However, in the absence of absolute information on yaw or position, the estimated state inevitably drifts over time.

5.2 Future Work

Several extensions can be considered to address the observed limitations:

- **Vertical state constraints:** The persistent drift in the vertical position suggests the need for additional measurements or assumptions, such as barometric altitude, rangefinders or similar.

- **Yaw stabilization during low excitation:** Incorporating complementary heading information, for example, from magnetometers, vision-based estimates, or richer radar measurements, could reduce yaw drift during near-stationary motion.

- **Exact discretization of error dynamics:** The current implementation uses a first-order approximation for discretizing the continuous-time error-state model. Applying exact discretization methods, such as Van Loan's method, may improve numerical consistency, particularly for larger sampling intervals.

- **Adaptive measurement handling:** Adaptive gating could improve performance during periods with sparse or noisy radar returns without discarding informative measurements.

These directions represent natural extensions of the current work and are expected to improve robustness and estimation accuracy in future implementations.

Appendix

A TI xWR68xx radar configuration

```
1   % Radar configuration for Radar Inertial Datasets ICINS 2021
2   % If you use this config for your academic research, please cite our related paper:
3   % C.Doer, G.F.Trommer: Yaw aided Radar Inertial Odometry uisng Manhattan World Assumptions;
    ↪  ICINS2021
4   %
5   % Generated Chirp
6   % d_max_final : 20.00 m
7   % d_res_final : 0.07 m
8   % d_interbin : 0.08 m
9   % v_max_final: 4.00 m/s
10  % v_res_final: 0.13 m/s
11  % v_interbin: 0.12 m/s
12  %
13  % Chirp Params
14  % N_range: 256
15  % N_frames: 60
16  % N_velocity_fft: 64
17  % T_f : 18.39 ms
18  % T_c : 102.19 us
19  % T_ramp : 63.75 us
20  % T_idle : 38.44 us
21  % T_adc_valid : 7.00 us
22  % T_adc_end_margin : 2.00 us
23  % f_sample : 4675.80 ksps
24  % S : 35.04 MHz/us
25  % B : 2.23 GHz
26  % radar_cube_size : 786.43 KB
27  % Config
28  %
29  sensorStop
30  flushCfg
31  dfeDataOutputMode 1
32  channelCfg 15 7 0
33  adcCfg 2 1
34  adcbufCfg -1 0 1 1 1
35  profileCfg 0 60.00 38.44 7.00 63.75 0 0 35.04 1.00 255 4675.80 0 0 30
36  chirpCfg 0 0 0 0 0 0 0 1
37  chirpCfg 1 1 0 0 0 0 0 2
38  chirpCfg 2 2 0 0 0 0 0 4
39  frameCfg 0 2 60 0 100.0 2 0.00
40  lowPower 0 0
41  guiMonitor -1 1 0 0 0 0 1
42  cfarCfg -1 0 2 8 4 3 0 8 0
43  cfarCfg -1 1 0 4 2 3 1 20 1
44  multiObjBeamForming -1 1 0.5
45  clutterRemoval -1 0
46  aoaFovCfg -1 -90 90 -90 90
47  cfarFovCfg -1 0 0.1 19.0
48  cfarFovCfg -1 1 -8.00 8.00
49  calibDcRangeSig -1 0 -5 8 256
50  extendedMaxVelocity -1 0
51  lvdsStreamCfg -1 0 0 0
52  measureRangeBiasAndRxChanPhase 0 1.5 0.2
53  compRangeBiasAndRxChanPhase 0.0 1 0 -1 0 1 0 -1 0 1 0 -1 0 1 0 -1 0 1 0 -1 0 1 0 -1 0
54  CQRxSatMonitor 0 3 5 103 0
55  CQSigImgMonitor 0 95 6
56  analogMonitor 0 0
57  calibData 0 0 0
58  sensorStart
```

Listing 1: TI xWR68xx AOP radar CLI configuration used for all experiments [18].

B   Alignment with UN Sustainable Development Goals

This project contributes to enabling robust autonomous navigation in environments where GNSS and vision-based sensing are unreliable, such as low-visibility or obstructed conditions. Reliable state estimation under such conditions is a key enabler for safe and effective deployment of autonomous systems.

The work aligns most directly with **SDG 9 (Industry, Innovation and Infrastructure)**, specifically Target 9.5, which is about enhancing scientific research. By supporting resilient robotics and autonomy for inspection, monitoring, and operation in challenging environments. Improved localization robustness can reduce operational risk and increase reliability in industrial and infrastructural applications.

The project also relates to **SDG 3 (Good Health and Well-being)**, as robust autonomy can enable remote operation in environments that are hazardous or inaccessible to humans, potentially improving safety. While this work does not directly address environmental or societal challenges, it provides foundational technology that can support autonomous systems used in such contexts.

References

[1] Ali Rida Sahili et al. 'A Survey of Visual SLAM Methods'. In: *IEEE Access* 11 (2023), pp. 139643–139677. DOI: 10.1109/ACCESS.2023.3341489.

[2] Kyle Harlow et al. 'A New Wave in Robotics: Survey on Recent MmWave Radar Applications in Robotics'. eng. In: *IEEE transactions on robotics* 40 (2024), pp. 4544–4560. ISSN: 1552-3098.

[3] Morten Nissov et al. 'Robust High-Speed State Estimation for Off-Road Navigation Using Radar Velocity Factors'. In: *IEEE Robotics and Automation Letters* 9.12 (2024), pp. 11146–11153. DOI: 10.1109/LRA.2024.3486189.

[4] Morten Nissov, Nikhil Khedekar and Kostas Alexis. *Degradation Resilient LiDAR-Radar-Inertial Odometry*. 2024. arXiv: 2403.05332 [cs.RO]. URL: https://arxiv.org/abs/2403.05332.

[5] Sarah Cen and Paul Newman. 'Radar-only ego-motion estimation in difficult settings via graph matching'. In: May 2019, pp. 298–304. DOI: 10.1109/ICRA.2019.8793990.

[6] Changseung Kim et al. 'EKF-Based Radar-Inertial Odometry with Online Temporal Calibration'. In: *arXiv preprint arXiv:2502.00661* (2025).

[7] Texas Instruments. *mmWave radar sensors*. 2025. URL: https://www.ti.com/product-category/sensors/mmwave-radar/overview.html (visited on 11th Dec. 2025).

[8] Cesar Iovescu and Sandeep Rao. *The fundamentals of millimeter wave radar sensors (Rev. A)*. Tech. rep. Texas Instruments, 2020. URL: https://www.ti.com/lit/wp/spyy005a/spyy005a.pdf (visited on 10th Dec. 2025).

[9] Paulina Rowińska. *What Is a Manifold?* 2025. URL: https://www.quantamagazine.org/what-is-a-manifold-20251103/ (visited on 10th Dec. 2025).

[10] Joan Solà, Jeremie Deray and Dinesh Atchuthan. *A micro Lie theory for state estimation in robotics*. 2021. arXiv: 1812.01537 [cs.RO]. URL: https://arxiv.org/abs/1812.01537.

[11] Joan Solà. *Quaternion kinematics for the error-state Kalman filter*. 2017. arXiv: 1711.02508 [cs.RO]. URL: https://arxiv.org/abs/1711.02508.

[12] Timothy D. Barfoot. *State Estimation for Robotics*. Cambridge University Press, 2017.

[13] Edmund Brekke. *Fundamentals of Sensor Fusion, Fifth Edition*. Edmund Brekke, 2024.

[14] VectorNav. *VN-100 IMU/AHRS*. 2024. URL: https://www.vectornav.com/docs/default-source/product-brief/vn-100-product-brief.pdf (visited on 11th Dec. 2025).

[15] Texas Instruments. *IWR6843AOP evaluation module for single-chip 60GHz antenna-on-package (AoP) mmWave sensor*. URL: https://www.ti.com/tool/IWR6843AOPEVM (visited on 16th Dec. 2025).

[16] James Stewart. *Calculus: Early Transcedentals*. Cengage Learning, 2015.

[17] Michael Grupp. *evo: Python package for the evaluation of odometry and SLAM*. 2025. URL: https://github.com/MichaelGrupp/evo/wiki/evo_traj (visited on 16th Dec. 2025).

[18] Christopher Doer and Gert F. Trommer. 'Yaw aided Radar Inertial Odometry uisng Manhattan World Assumptions'. In: *2021 28th Saint Petersburg International Conference on Integrated Navigation Systems (ICINS)*. 2021.